INTERNATIONAL JOURNAL FOR NUMERICAL METHODS IN FLUIDS
Int. J. Numer. Meth. Fluids 2008; **58**:639–658

A pseudospectral Fourier method for a 1D incompressible two-fluid model

H. Holmås[1, *, †], D. Clamond[2] and H. P. Langtangen[3, 4]

[1] *Scandpower Petroleum Technology, P.O. Box 113, 2027 Kjeller, Norway*
[2] *Institute for Energy Technology, P.O. Box 40, 2027 Kjeller, Norway*
[3] *Simula Research Laboratory, P.O. Box 134, 1325 Lysaker, Norway*
[4] *Department of Informatics, University of Oslo, P.O. Box 1080 Blindern, N-0316 Oslo, Norway*

SUMMARY

This paper presents an accurate and efficient pseudospectral (PS) Fourier method for a standard 1D incompressible two-fluid model. To the knowledge of the authors, it is the first PS method developed for the purpose of modelling waves in multiphase pipe flow. Contrary to conventional numerical methods, the PS method combines high accuracy and low computational costs with flexibility in terms of handling higher order derivatives and different types of partial differential equations. In an effort to improve the description of the stratified wavy flow regime, it can thus serve as a valuable tool for testing out new two-fluid model formulations. The main part of the algorithm is based on mathematical reformulations of the governing equations combined with extensive use of fast Fourier transforms. All the linear operations, including differentiations, are performed in Fourier space, whereas the nonlinear computations are performed in physical space. Furthermore, by exploiting the concept of an integrating factor, all linear parts of the problem are integrated analytically. The remaining nonlinear parts are advanced in time using a Runge–Kutta solver with an adaptive time step control. As demonstrated in the results section, these steps in sum yield a very accurate, fast and stable numerical method. A grid refinement analysis is used to compare the spatial convergence with the convergence rates of finite difference (FD) methods of up to order six. It is clear that the exponential convergence of the PS method is by far superior to the algebraic convergence of the FD schemes. Combined with the fact that the scheme is unconditionally linearly stable, the resulting increase in accuracy opens for several orders of magnitude savings in computational time. Finally, simulations of small amplitude, long wavelength sinusoidal waves are presented to illustrate the remarkable ability of the PS method to reproduce the linear stability properties of the two-fluid model.

Received 18 July 2007; Revised 5 December 2007; Accepted 2 January 2008

KEY WORDS: pseudospectral; numerical methods; waves; two-fluid models

---

[*] Correspondence to: H. Holmås, Scandpower Petroleum Technology, P.O. Box 113, 2027 Kjeller, Norway.
[†] E-mail: havard.holmas@sptgroup.com

Contract/grant sponsor: Horizon Joint Industry Program

1. INTRODUCTION

One-dimensional two-fluid models are commonly used to describe multiphase transport of hydrocarbons in pipe lines. Despite the recent increase in interest for the stratified wavy flow regime, the prevailing models do not predict the properties of the corresponding large waves satisfactorily. Since no nontrivial analytical solutions are available, numerical simulations combined with physical experiments represent the only way to test out improvements in two-fluid models. It is thus crucial to have accurate numerical methods capable of capturing the true mathematical behavior of the model equations. By doing so, the physical effects of new mathematical terms can be identified and compared with experimental observations. While conventional methods often introduce excessive numerical errors in the solution, pseudospectral (PS) methods [1–3] are known to be both very accurate and efficient. Furthermore, they are already well established as a successful numerical tool within, for example, turbulence, meteorology and ocean waves. This paper presents a PS Fourier method adapted to the 1D incompressible two-fluid model. It is demonstrated that these methods also have a great potential for modelling waves in multiphase pipe flow.

The main principles used in PS methods were first introduced by Galerkin [4]. When applied to partial differential equations (PDEs), the main idea is to approximate the solution by a (truncated) series of differentiable basis functions. The spatial derivatives of this approximation are then evaluated analytically. In essence, this approach ensures that information from the whole computational domain is included every time a spatial derivative is computed. In finite element and finite difference (FD) methods, on the other hand, spatial derivatives are computed using information only from a few neighboring grid points. Finally, the PS spatial scheme is combined with an ordinary differential equation (ODE) solver in order to march the solution forward in time.

Although many different options exist, the by far most popular choice of basis functions is to use a Fourier series expansion of the solution. The main advantage of this approach is due to the superior computational efficiency of the fast Fourier transform (FFT). Kreiss and Oliger [5] and Orszag [6] were the first to apply PS methods to PDEs. Their approach early became popular within weather prediction and simulation of turbulence, and these fields have contributed strongly to the development of new algorithms from the late 1970s up until today. Currently, the main strengths of the PS methods include exponential as opposed to (much slower) polynomial error decay rates, minimal dispersive and dissipative errors, and flexibility with respect to treatment of nonlinearities and higher order derivatives [3]. Moreover, due to the low number of grid points required to uphold accuracy, very fast and memory efficient algorithms can be constructed. There are, however, still some unresolved issues related to certain boundary conditions, irregular geometries and strong shocks in the solutions. All the same, ever more of these limitations are overcome, and the list of scientific fields that embrace PS methods is continuously growing [7].

The main motivation behind the present work is to provide a numerical framework for testing out improvements in 1D incompressible two-fluid models for multiphase pipe flow. In particular, the method should be suitable for simulations of large waves (roll waves) in stratified flow. This flow regime is observed in laboratory experiments [8], and it is believed to be especially important in large diameter gas-condensate pipelines. Nevertheless, to our knowledge, there exists no transient 1D two-fluid model that is able to predict stable waves [9]. Since the stability and evolution of waves are very sensitive to numerical errors, accuracy was the most important property in our search for a suitable numerical method. The leading commercial simulators for multiphase pipe flow are mainly based on low-order numerical methods and coarse grids combined with some sort of tracking schemes [10–12]. Correlations are used to determine the flow regimes, and

DOI: 10.1002/fld

different flow models are applied in the different regimes. These codes are thus excellent tools for simulating the flow in long pipelines with complex geometries, but they are not suitable for predicting the detailed development of waves. Lately, Omgba-Essama [13] and Issa and Kempf [14] among others have attempted to capture slug initiations by resolving instabilities in two-fluid models. Their numerical approach is based on using fine grids in combination with first- and second-order discretizations. While such discretization schemes are more robust with respect to handling discontinuities in the solutions, it will be shown in this paper that they are not as accurate and efficient as PS methods when it comes to simulating waves. Finally, Barnea and Taitel [9] used high-resolution methods based on characteristics to study nonlinear waves in the hyperbolic region of the two-fluid model. To open for investigation of all flow conditions and higher order derivatives in the equations, however, it was essential that our method was able to handle all types of PDEs relevant for two-fluid models. Thereby, all schemes requiring exclusively real and positive characteristics were ruled out as well.

A PS method was thus considered to be the most attractive alternative. Besides their superior properties with respect to simulating waves in 1D two-fluid models, PS methods could also be used to simulate the stratified flow regime in a complete pipe flow simulator. Such an application is, however, outside the scope of the work presented in this paper. The particular PS algorithm we have used was preferred due to the success of a similar approach constructed by Fructus *et al.* [15] for nonlinear waves in free surface flows. Owing to the different natures of the two problems, however, significant modifications in the solution strategy were necessary. Although being based on known concepts, the result is thus a novel numerical method. Furthermore, to our knowledge, it is the first PS method developed for the modelling of waves in multiphase pipe flow.

Section 2 presents the two-fluid model, for which the PS method has been developed. Additionally, the Korteweg–de Vries (KdV) equation, which is used as a complementary test case, is introduced. In the following section, the numerical method is described. A brief overview of the steps in the algorithm is given first, and thereafter the most central elements are discussed in further detail. Finally, Section 4 presents the simulation results before the paper is concluded in Section 5.

2. MODEL EQUATIONS

This section introduces the two wave models that are solved numerically in Section 4. The main model is a standard 1D incompressible two-fluid model for multiphase pipe flow. To open for a more complete evaluation of the PS method, however, a simpler two-fluid model called the Korteweg–de Vries (KdV) equation is considered as well. Similar to the main two-fluid model, the KdV equation models long waves in shallow water. This similarity together with the fact that it has a known analytical travelling wave solution makes the KdV equation very suitable as a numerical test problem. Moreover, the KdV equation also contains a higher order derivative, which is relevant with respect to inclusion of dissipative or dispersive effects in the two-fluid model.

2.1. The two-fluid model

The incompressible two-fluid model used in this paper consists of two PDEs and two algebraic relations. This particular formulation was originally derived by Watson [16], but it is mathematically equivalent to standard two-fluid models used widely in the literature [17, 18]. Note that for typical separated flows the speed of the mass waves that we are interested in is about two orders of magnitude slower than the speed of sound. To study these slow transients, it is thus considered reasonable to assume local equilibrium in the pressure wave system and use incompressible models. Any model improvements can subsequently be transferred by analogy to their compressible counterparts, which must be used in order to describe other important multiphase phenomena such as severe slugging or flows with more mixing.

The two PDEs consist of the liquid continuity equation

$$(\alpha_{\rm l})_t + (\alpha_{\rm l} u_{\rm l})_x = 0 \tag{1}$$

and the balance equation for the slip momentum

$$v_t + [\tfrac{1}{2}\rho_{\rm l} u_{\rm l}^2 - \tfrac{1}{2}\rho_{\rm g} u_{\rm g}^2 + (\rho_{\rm l} - \rho_{\rm g}) h_{\rm l} g \cos\beta]_x = S \tag{2}$$

Here, S denotes the source terms given by

$$S \equiv -\frac{\tau_{\rm l} s_{\rm l}}{\alpha_{\rm l} A} + \frac{\tau_{\rm g} s_{\rm g}}{\alpha_{\rm g} A} + \left(\frac{1}{\alpha_{\rm l} A} + \frac{1}{\alpha_{\rm g} A}\right)\tau_{\rm i} s_{\rm i} - (\rho_{\rm l} - \rho_{\rm g})(g \sin\beta) \tag{3}$$

and the slip momentum is defined by $v \equiv \rho_{\rm l} u_{\rm l} - \rho_{\rm g} u_{\rm g}$. Subscripts l, g and i represent the liquid phase, the gas phase and the interface, respectively. Furthermore, ρ denotes the density, α the phase fraction, u the velocity, g the acceleration of gravity, h the phase height, A the cross-sectional area of the pipe, τ the shear stress, s the wetted perimeter, and β the pipe inclination (assumed constant). The notation is illustrated in Figure 1.

The first algebraic equation is the geometric constraint

$$\alpha_{\rm l} + \alpha_{\rm g} = 1 \tag{4}$$

and the second one is a relation describing the total volume flux of the flow

$$\alpha_{\rm l} u_{\rm l} + \alpha_{\rm g} u_{\rm g} = U_{\rm m}(t) \tag{5}$$

The mixture velocity, $U_{\rm m}$, is a spatial integration constant and an input parameter to the problem. For the simulations presented in this paper, it is constant not only in space but also in time.

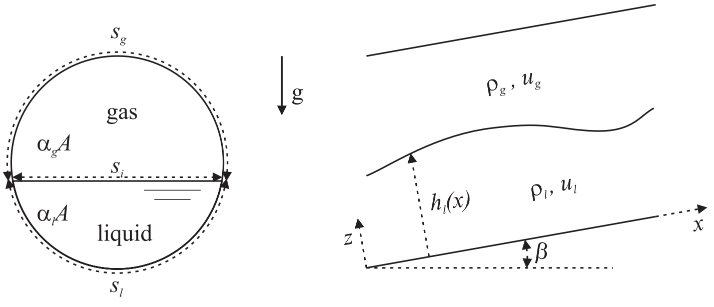

Figure 1. Sketch of the flow geometry.

DOI: 10.1002/fld

Furthermore, important underlying assumptions of model (1)–(5) include the long wavelength assumption leading to hydrostatic pressure distributions in the phases, constant phase densities, no transverse variation of the velocities (plug flow) and no mass transfer.

Using the algebraic relations (4) and (5) together with the definition of the slip velocity, the gas phase fraction and the velocities can be found as functions of the dependent variables:

$$\alpha_{\mathrm{g}}=1-\alpha_{\mathrm{l}},\quad u_{\mathrm{l}}=\frac{v(1-\alpha_{\mathrm{l}})+\rho_{\mathrm{g}}U_{\mathrm{m}}}{\rho_{\mathrm{l}}(1-\alpha_{\mathrm{l}})+\rho_{\mathrm{g}}\alpha_{\mathrm{l}}}\quad \text{and}\quad u_{\mathrm{g}}=\frac{-v\alpha_{\mathrm{l}}+\rho_{\mathrm{l}}U_{\mathrm{m}}}{\rho_{\mathrm{l}}(1-\alpha_{\mathrm{l}})+\rho_{\mathrm{g}}\alpha_{\mathrm{l}}} \tag{6}$$

Finally, closure models must be provided for the shear stresses τ_{l}, τ_{g} and τ_{i}. In the present work, a friction factor relation based on the single-phase Haaland formula is used. The defining equations are given in Appendix A, and Espedal [19] can be consulted for a detailed discussion of the model.

For brevity, the following matrix notation will be used throughout the rest of this paper

$$\mathbf{\Psi}_t=\mathbf{A}(\mathbf{\Psi}) \tag{7}$$

where $\mathbf{\Psi}$ is the vector containing the dependent variables, $\mathbf{\Psi}\equiv\binom{\alpha_{\mathrm{l}}}{v}$ and $\mathbf{A}$ is an operator defined by

$$\mathbf{A}(\mathbf{\Psi})\equiv\begin{pmatrix} -(\alpha_{\mathrm{l}}u_{\mathrm{l}})_x \\ -[\frac{1}{2}\rho_{\mathrm{l}}u_{\mathrm{l}}^2-\frac{1}{2}\rho_{\mathrm{g}}u_{\mathrm{g}}^2+(\rho_{\mathrm{l}}-\rho_{\mathrm{g}})h_{\mathrm{l}}g\cos\beta]_x+S \end{pmatrix} \tag{8}$$

2.2. *The KdV equation*

The KdV equation is a model equation for 1D shallow water waves in rectangular channels [20, 21]. In dimensional form, it can be expressed as

$$\eta_t+c_0\eta_x+\tfrac{1}{6}c_0h_0\eta_{xxx}=-\tfrac{3}{4}c_0h_0^{-1}(\eta^2)_x \tag{9}$$

where η denotes the surface elevation relative to the mean liquid height, h_0, and $c_0\equiv\sqrt{gh_0}$ is the critical wave speed. A dimensionless form is obtained by scaling the equation with h_0 and g. Technically, the resulting equation corresponds to setting $h_0=g=1$ in (9), and it is this formulation that is used in the simulations in Section 4.

While the nonlinear term on the right-hand side of (9) drives waves towards breaking, the third-order dispersive term on the left-hand side tends to stretch the waves out and form wave trains. It is the balance between these two opposing effects that opens for the travelling wave solution to the KdV equation. As mentioned, this solution can be obtained analytically, and it takes the form of a gravity-driven cnoidal wave [20] that propagates downstream without changing shape. The exact analytical expression for the surface elevation is given in Appendix B. Besides serving as a benchmark for the numerical solutions to the KdV equation, the cnoidal wave is also used in the initial conditions for some of the two-fluid model simulations in Section 4.

3. NUMERICAL ALGORITHM

This section presents our PS numerical method for the incompressible two-fluid model defined by (7). Since descriptions of similar PS methods for the KdV equation already exist in the

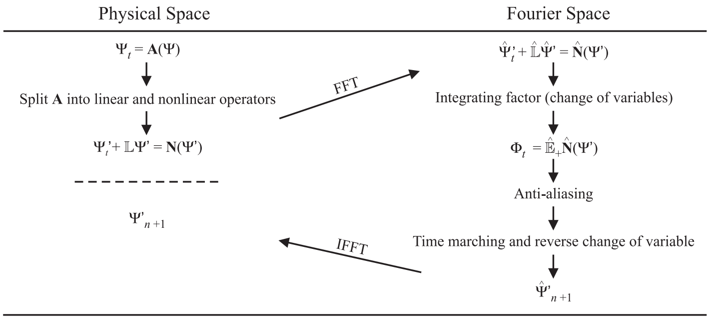

Figure 2. Schematic illustration of the steps in the PS method. Subscript t denotes time derivatives, subscript $n+1$ indicates the next time step, apostrophes indicate the varying parts of variables and hats are used for variables in Fourier space.

literature [2, 22]; that procedure will not be described here. Nonetheless, by analogy most of the implementations for the KdV equation follow the two-fluid model algorithm.

Partly based on the ideas introduced by Fornberg and Whitham [22], Fructus *et al.* [15] constructed a very fast and accurate PS method for nonlinear ocean waves. In essence, many of the same steps are used in the numerical method presented here, but several modifications of the numerics and the model itself are necessary in order to adapt the approach to the two-fluid model. In contrast to the model equations for ocean waves, linear and nonlinear effects are not separated in standard two-fluid models. Since an important part of the solution strategy is to solve the linear parts analytically, our method has an extra initial step mainly concerned with extracting the linear terms from (7). Furthermore, the solution strategy is to a great extent based on mathematical reformulations. These reformulations thus have to be derived for the two-fluid model, and many adjustments must be made throughout the numerical method. Hence, the result is a new PS algorithm customized for the simulation of waves in multiphase pipe flow.

Figure 2 visualizes the main steps in this PS method. As mentioned, the equation set is first split into linear and nonlinear terms. Thereafter, the nonlinear operations are carried out before the equation set is transformed into Fourier space. This transformation indirectly takes care of the periodic boundary conditions as well as the spatial derivatives, which in Fourier space are computed by simple multiplications. Next, a change of variables that ensures that the analytical integration of the linear parts of the system is applied. In order to avoid instabilities caused by the nonlinear operations, a cut-off is applied to the high frequencies of the solution. After this so-called anti-aliasing procedure, the remaining nonlinear parts are marched forward in time using a fifth-order Runge–Kutta method with adaptive time stepping. Finally, the solution at the next time step is obtained by reversing the change of variables and transforming back to physical space. The rest of this section discusses these steps in further detail.

3.1. Splitting of linear and nonlinear terms

Inspection of (7) reveals that all terms except the temporal derivatives and the gravity term are nonlinear with respect to the dependent variables $\boldsymbol{\Psi}$. Further linear parts can, however, be extracted by reformulating the original equations. To do so, first-order Taylor expansions about a mean state are employed. The dependent variables are first rewritten as a sum of this mean state and a deviation

$$\boldsymbol{\Psi} \equiv \boldsymbol{\Psi}_0 + \boldsymbol{\Psi}' \equiv \begin{pmatrix} \alpha_{\mathrm{l}0} \\ v_0 \end{pmatrix} + \begin{pmatrix} \alpha_{\mathrm{l}}' \\ v' \end{pmatrix} \tag{10}$$

In view of the numerical method, the mean state, $\boldsymbol{\Psi}_0$, must be constant in space, but not necessarily in time. However, due to the physics involved in this particular problem (constant mixture velocity and periodic boundary conditions), the mean state is constant in both space and time. Furthermore, this constant is dictated by the initial conditions, and in all simulations presented in this paper it will correspond to the uniform steady-state solution to (7). Since the temporal and spatial derivatives of $\boldsymbol{\Psi}_0$ thus equal zero, the deviations, $\boldsymbol{\Psi}'$, become the new dependent variables of the equation system. Such a formulation not only minimizes the round-off errors but also better reflects the physical behavior of the flow.

Next, first-order Taylor expansions are applied to the rest of the variables in order to extract all the terms that are linear in the new dependent variables. The remainders of the expansions are retained in the equations and treated as nonlinear terms. Hence, the resulting equation set is mathematically identical to (7). The only difference is that the operator **A** has been split into a linear operator, $\mathbb{L}$, and a nonlinear operator, **N** (see Equation (13)).

In the liquid continuity equation (1), the only variable that needs to be expanded is the liquid velocity

$$u_{\mathrm{l}} = u_{\mathrm{l}0} + u_{\mathrm{l}}' = u_{\mathrm{l}0} + \alpha_{\mathrm{l}}' \left(\frac{\partial u_{\mathrm{l}}}{\partial \alpha_{\mathrm{l}}} \right)_{\boldsymbol{\Psi}_0} + v_{\mathrm{l}}' \left(\frac{\partial u_{\mathrm{l}}}{\partial v_{\mathrm{l}}} \right)_{\boldsymbol{\Psi}_0} + R_{u_{\mathrm{l}}} \tag{11}$$

Here, $u_{\mathrm{l}0} \equiv u_{\mathrm{l}}(\boldsymbol{\Psi}_0)$ and $R_{u_{\mathrm{l}}}$ denotes the remainder of the expansion. The short-form notation u_{l}' is used in terms that are nonlinear in the dependent variables. Furthermore, the expressions for the derivatives can be found from the algebraic relations in (6), and the subscript $\boldsymbol{\Psi}_0$ indicates that they are to be evaluated at the uniform steady-state conditions.

Introducing the notation from (10) and (11), the liquid continuity equation is rewritten as

$$\frac{\partial \alpha_{\mathrm{l}}'}{\partial t} + \left[\alpha_{\mathrm{l}0} \left(\frac{\partial u_{\mathrm{l}}}{\partial \alpha_{\mathrm{l}}} \right)_{\boldsymbol{\Psi}_0} \frac{\partial}{\partial x} + u_{\mathrm{l}0} \frac{\partial}{\partial x} \right] \alpha_{\mathrm{l}}' + \left[\alpha_{\mathrm{l}0} \left(\frac{\partial u_{\mathrm{l}}}{\partial v} \right)_{\boldsymbol{\Psi}_0} \frac{\partial}{\partial x} \right] v' = -\frac{\partial u_{\mathrm{l}}' \alpha_{\mathrm{l}}'}{\partial x} - \alpha_{\mathrm{l}0} \frac{\partial R_{u_{\mathrm{l}}}}{\partial x} \tag{12}$$

in which the nonlinear terms are collected on the right-hand side. Having extracted all the linear terms, (12) is now transformed into Fourier space. There, the first-order spatial derivatives are computed by multiplying the transformed variable with $\mathrm{i}k$, where $\mathrm{i}^2 = -1$ and k is the wave number. Note that periodic boundary conditions are automatically taken care of when using Fourier transforms. Other boundary conditions can be implemented by using transforms with a different set of basis functions [2].

After applying the same approach to the slip momentum equation (2), the equation set becomes

$$\hat{\boldsymbol{\Psi}}_t' + \hat{\mathbb{L}} \hat{\boldsymbol{\Psi}}' = \hat{\mathbf{N}}(\boldsymbol{\Psi}') \quad \text{with} \quad \hat{\mathbb{L}} = \begin{bmatrix} \hat{l}_{11} & \hat{l}_{12} \\ \hat{l}_{21} & \hat{l}_{22} \end{bmatrix} \quad \text{and} \quad \hat{\mathbf{N}}(\boldsymbol{\Psi}') = \begin{bmatrix} \hat{n}_1 \\ \hat{n}_2 \end{bmatrix} \tag{13}$$

where the hats indicate Fourier transforms. The expressions for the linear operator $\hat{\mathbb{L}}$ and the nonlinear operator $\hat{\mathbf{N}}(\boldsymbol{\Psi}')$ are given in Appendix C.

DOI: 10.1002/fld

3.2. Integrating factor

In order to integrate the linear terms in (13) analytically, a change of variables using an integrating factor is applied [2, 23]. Besides improving the accuracy, the main gain of the integrating factor approach is that the system becomes unconditionally linearly stable. Especially when higher order derivatives are involved, the computational time can thus be reduced by several orders of magnitude (see Section 4.2).

The following new variables are introduced:

$$\mathbf{\Phi} \equiv \mathbb{E}_+ \hat{\mathbf{\Psi}}' \;\Leftrightarrow\; \hat{\mathbf{\Psi}}' = \mathbb{E}_- \mathbf{\Phi} \tag{14}$$

where

$$\mathbb{E}_\pm \equiv \exp[\pm \hat{\mathbb{L}}(t-t_0)] \quad \text{with } \mathbb{E}_\pm = \begin{bmatrix} e_{\pm 11} & e_{\pm 12} \\ e_{\pm 21} & e_{\pm 22} \end{bmatrix} \tag{15}$$

is known as the integrating factor. In the numerical algorithm, t denotes the current time, and t_0 denotes the time at the beginning of the current time step. Since numerical computation of the exponential of a matrix is costly, the analytical expressions for the elements in $\mathbb{E}_\pm$ are used instead (see Appendix D). Finally, (14) is inserted into (13), and all linear parts cancel. The result, after some rearranging, is the following ODEs:

$$\mathbf{\Phi}_t = \mathbb{E}_+ \hat{\mathbf{N}}(\mathbf{\Psi}') \tag{16}$$

A few remarks to (16) are in place. First of all, the terms in $\hat{\mathbb{L}}$ are constant in time and thus have to be computed only once. The terms in $\hat{\mathbf{N}}(\mathbf{\Psi}')$, on the other hand, are functions of the dependent variables and must thus be reevaluated at each time step. Furthermore, no linear terms have been extracted from the source terms (3) in the slip momentum equation. Owing to the complex algebraic relations in the friction terms, it would be necessary to compute the resulting derivatives numerically. This procedure has been tried out, but the effects on the horizontal flow simulations presented in this paper were insignificant. The reason is probably a combination of the friction terms being dominated by nonlinear effects and the inaccuracy in the approximations of the derivatives. Finally, we would like to stress the importance of making sure that the mean of the initial conditions really corresponds to the mean state $\mathbf{\Psi}_0$. Any deviations would introduce errors in the Taylor expansions resulting in a loss of both accuracy and stability. In the simulations in Section 4, this issue is taken care of by using only initial perturbations on the uniform steady-state solutions that have zero mean values.

3.3. Anti-aliasing

At this point no further mathematical reformulations are feasible, and Equation (16) is integrated numerically. Before presenting the ODE solver, however, we will first describe the anti-aliasing procedure [1, 2], which is used throughout the numerical method. The purpose of this procedure is to control the aliasing errors introduced by nonlinear computations on discrete grids. Consider, for example, the multiplication of two functions in physical space. In the continuous case, such an operation corresponds to a convolution in Fourier space, whereas in the discrete case, it corresponds to a *circular* convolution. In other words, the discretization of a product is not the same as the product of discretized functions. The resulting aliasing errors manifest themselves by destabilizing high wave numbers in the discretized solution spectrum. Note that aliasing errors is not something peculiar to PS methods. However, most other schemes also introduce so much numerical dissipation that all the energy at high wave numbers is damped. The aliasing errors are thus eliminated, but so are parts of the physics.

An attractive anti-aliasing procedure for 1D simulations, which are not memory intensive, is to extend the high wave number part of the solution spectrum by zeros padding [2]. For a nonlinearity of order r_n, the required extension of the spectrum is by a factor of $(r_n+1)/2$. It is troublesome to find the order of all the nonlinearities in (16). However, our conclusion after careful investigations of different solution spectra is that application of the $\frac{4}{2}$-rule [2, 15] is sufficient to suppress the aliasing errors. The strategy we have used for nonlinear operations thus consists of two parts, which are both carried out for every nonlinear operation at every time step. Since multiplications are much faster to compute than convolutions, all nonlinearities are first evaluated in physical space. Thereafter, the solution is transformed into Fourier space, and the upper half of its spectrum is set equal to zero. Many transforms between the two spaces are thus necessary. Thanks to the speed of the FFT algorithms, however, the computational cost is minimal.

3.4. Numerical integration

Many suitable ODE solvers exist in the literature [24]. In order to solve (16) in a satisfactory way, there are especially two properties that the solver should possess. Firstly, a medium-to-high range accuracy is required so that the accuracy of the spatial discretization is not deteriorated. Secondly, an adaptive step size control should be used. This feature is quite effortless to implement, and it can reduce the computational time substantially [25].

Based on these criteria, we have chosen to use a well-known Runge–Kutta method by Dormand and Prince [26]. It is a six stage, fifth-order explicit method with an embedded fourth-order scheme for the time stepping control. Note that when using the integrating factor, it is important to make sure that all variables are updated at each substep before (16) is used to calculate the temporal derivatives. For the time stepping, a proportional integral (PI) controller is used [27]. The estimated time step size is given by

$$\Delta t_{n+1} = \Delta t_n \left(\frac{1}{\mathrm{err}_n}\right)^a \left(\frac{\mathrm{err}_{n-1}}{\mathrm{err}_n}\right)^b \tag{17}$$

in which the constants a and b are subject to tuning. In the simulations presented here, $a=0.3/p$ and $b=0.4/p$ as recommended by Gustafsson [28]. The parameter p denotes the order of the scheme, which in our case is $p=5$. Furthermore, the error estimates are calculated from

$$\mathrm{err}_n = \sqrt{\frac{1}{2J}\sum_{i=1}^{2}\sum_{j=1}^{J}\left\{\frac{\mathbf{\Phi}_n(i,j)-\mathbf{\Phi}_n^{4\text{th}}(i,j)}{\mathrm{TOL}+\max[\mathbf{\Phi}_n(i,j),\mathbf{\Phi}_{n-1}(i,j)]\cdot\mathrm{TOL}}\right\}^2} \tag{18}$$

Subscripts $n-1$, n and $n+1$ indicate the time steps, superscript 4th represents the fourth-order embedded scheme, TOL denotes the tolerance in the Runge–Kutta solver and J is the total number of grid points in the simulation. As can be seen in (17), the PI controller, in contrast to traditional integral (I) controllers, includes the error estimates from both the current and the previous time steps when estimating the next time step size. Owing to the stiffness of multiphase flow problems, such a stabilization technique is very advantageous. By providing improved estimates of the step sizes, it can significantly reduce the number of rejected time steps and thereby also reduce the total computational time.

After each time step, Equation (14) is used to reverse the change of variables. Thereafter, the phase fractions and velocities are obtained by applying inverse FFT algorithms followed by the relations in (6). Thus, all terms at the new time step can be calculated, and the solution can be marched further forward in time.

4. SIMULATION RESULTS AND DISCUSSIONS

Through comparisons with a range of FD schemes, this section demonstrates the superior accuracy and efficiency of the PS method. The simulations are set up to model the flow of water ($\rho_l = 998\,\mathrm{kg/m^3}$, $\mu_l = 10^{-3}\,\mathrm{Pa\,s}$) and sulfurhexafluoride ($\rho_g = 50\,\mathrm{kg/m^3}$, $\mu_g = 1.61\times 10^{-5}\,\mathrm{Pa\,s}$) in a horizontal pipe with a diameter $D = 0.1$ m. Furthermore, the length of the periodic computational domain is $100D$, and the initial conditions are given by the uniform steady-state solution to (7) superposed by a zero mean perturbation. The flow rates and the form of the initial perturbations, however, vary among the different simulation cases. In order to enable comparison with an analytical solution and to demonstrate the efficiency of the integrating factor, some simulations with the KdV equation are included as well.

The FD schemes used as the basis for comparison are of orders 1, 2, 4 and 6. They use the same Runge–Kutta solver as the PS scheme, but the change of variables described in Section 3.2 is not included. While the spatial derivatives in the first-order scheme are discretized with ordinary backward differences, the spatial derivatives of the higher order schemes are computed in Fourier space. Thus, much of the code structure from the PS method is reused, and the comparisons become both more reliable and easier to implement. The Fourier versions of the ordinary central differences [3] are obtained by repeatedly employing the following formula:

$$\mathscr{F}\{f(x-a\Delta x)\} = \exp(-\mathrm{i}a\Delta x)\mathscr{F}\{f(x)\} \tag{19}$$

where f is some arbitrary function, a is a constant and $\mathscr{F}$ denotes the Fourier transform. All parts of the code have been implemented in the Matlab programming language. The standard library functions `fzero`, `fft` and `ifft` have been used to compute the uniform steady-state solution for the initial conditions, the FFTs and the inverse FFTs, respectively.

4.1. Accuracy and convergence

To analyze the accuracy and convergence rate of the PS scheme, simulations of both the two-fluid model and the KdV equation are used. In both cases an initial cnoidal wave is propagated a distance corresponding to twice the length of the periodic computational domains. For the two-fluid model simulations, the flow rates correspond to conditions for which Johnson [8] in his experimental work observed a stratified flow regime with roll waves. In particular, the superficial liquid velocity is $u_{sl} = 0.4\,\mathrm{m/s}$, and the superficial gas velocity is $u_{sg} = 2.0\,\mathrm{m/s}$ (see Figure 6(a)).

Figure 3 shows the qualitative behavior of the simulation results with 64 grid points. Panels a and b represent the KdV equation, whereas Panels c and d represent the two-fluid model simulations. Furthermore, Panels a and c show the temporal evolution of the PS solutions, whereas Panels b and d compare the final solution profiles of the different numerical methods. From Panel b it is evident that despite the low number of grid points, the PS method approximates the analytic solution to

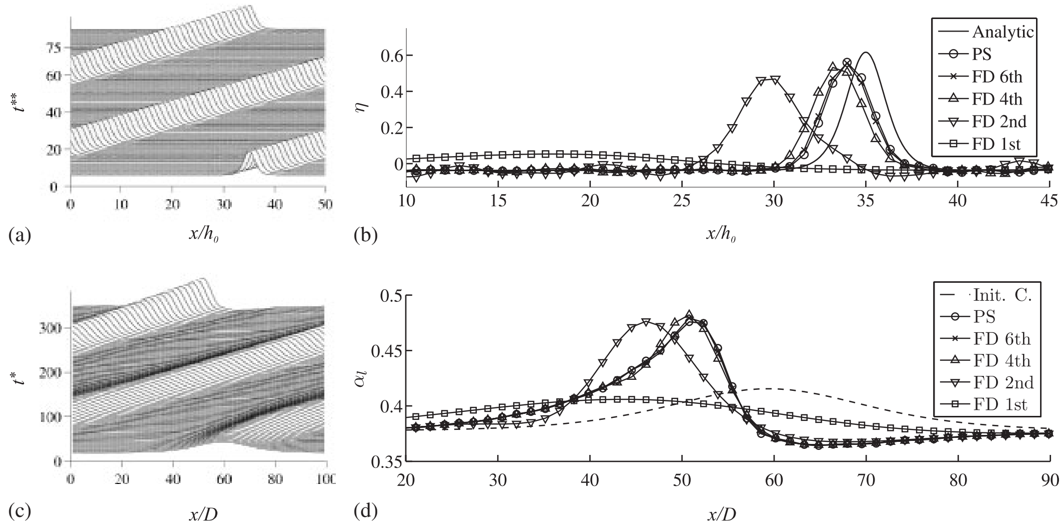

Figure 3. Temporal evolution of the PS simulations and sections of the final surface profiles for the KdV equation (Panels a and b) and the two-fluid model (Panels c and d), respectively. In all simulations, 64 grid cells were used, and the initial cnoidal wave was propagated about twice the distance of the periodic computational domain corresponding to $100h_0$ for the KdV equation and $200D$ for the two-fluid model. The dimensionless times are defined by $t^{**} \equiv t/\sqrt{gh_0}$ and $t^* \equiv t/(D/U_{\mathrm{m}})$.

the KdV equation well. It is hard to visually distinguish the PS method and the sixth-order FD method, but the rest of the FD methods clearly yield poorer results. Especially striking is the extent to which the first-order method smears out the solution and the considerable oscillations in the second-order solution.

While the initial wave essentially retains its shape throughout the simulation for the KdV equation, it can be seen in Panel c that the wave in the two-fluid model simulation both grows and gets closer to breaking. In fact, if the simulations were allowed to continue, the numerics would eventually blow up due to the developing shock discontinuity. As for the KdV equation, it is hard to distinguish the final holdup profiles of the PS and the sixth-order method in Panel d. Furthermore, the rest of the FD methods have the same tendency to smear out the solution and underpredict the phase speed.

A more quantitative analysis of the convergence rates is shown in Figure 4. An error estimate is calculated based on the final surface profiles in Figure 3, and a grid refinement analysis is carried out. The error estimate is defined by

$$\varepsilon(J) \equiv \sqrt{\frac{1}{J}\sum_{j=1}^{J} |\mathbf{v}_{\mathrm{b}}(j) - \mathbf{v}_J(j)|^2} \tag{20}$$

where $\mathbf{v}_J$ denotes the final surface vector with J grid points, and $\mathbf{v}_{\mathrm{b}}$ is the benchmark solution vector. For the KdV equation, the benchmark is given by the analytical solution to the surface elevation η. For the two-fluid model, on the other hand, a very refined PS numerical solution (5000

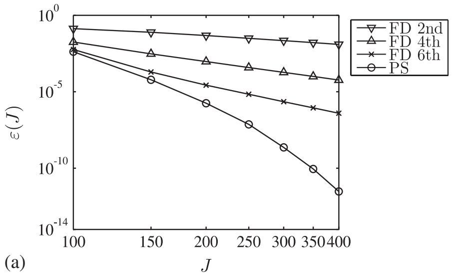

(b)

J_1 - J_2	p				q
	2nd	4th	6th	PS	PS
100 - 250	1.59	4.19	7.36	11.93	1.20
250 - 300	1.93	4.01	6.09	19.08	1.05
300 - 350	1.95	4.00	6.07	21.00	0.98
350 - 400	1.96	4.00	6.05	25.40	1.02

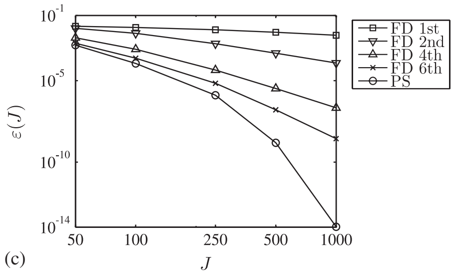

(d)

J_1 - J_2	p					q
	1st	2nd	4th	6th	PS	PS
50 - 100	0.23	1.03	2.35	3.04	3.52	0.47
100 - 250	0.34	1.60	3.20	3.87	4.43	0.42
250 - 500	0.48	1.95	3.77	5.41	8.66	0.55
500 - 1000	0.60	1.99	3.95	5.89	15.76	0.66

Figure 4. Plots of the error estimates and tables containing the convergence rates for the KdV simulations (Panels a and b) and the two-fluid model (Panels c and d). The algebraic order of convergence, p, is defined by (21), and the exponential convergence factor, q, is defined by (22).

grid points) to the holdup α_l is used. Once again the results for the KdV equation are given in Panels a and b, and the results for the two-fluid model are given in Panels c and d.

Based on the diagrams in Panels a and c, it is clear that the convergence rate of the PS method is by far superior to the rest of the schemes. Actually, the error for the PS method diminishes at an exponential rate, which is much faster than the algebraic rates obtained by FD methods. In order to quantify the convergence rates, the estimated order of convergence for each refinement interval is computed. The algebraic orders are defined as p in the following relations [2]:

$$\varepsilon_J \propto \frac{1}{J^p} \quad \text{for } J \to \infty \tag{21}$$

Since logarithmic scales are used, the algebraic orders correspond to the asymptotic slopes of the curves for large J. The exponential convergence factor, on the other hand, is defined by q in the following relations [2]:

$$\varepsilon_J \propto \exp(-cJ^q) \quad \text{for } J \to \infty \tag{22}$$

with c representing some constant.

The results of the computations are reported in the tables on the right-hand side of Figure 4. As anticipated, the orders of convergence for the FD methods approach their respective discretization orders for increasing J. The p-values for the PS method are reported in the tables as well. It can be seen that these values are continuously increasing with J, which explains why PS methods often are referred to as infinite order methods. A more proper measure of the exponential convergence, however, is provided by the q-values. An exponential convergence factor $q=1$ indicates geometric convergence, whereas $q<1$ and $q>1$ indicate subgeometric and supergeometric convergences, respectively. When approximating a smooth and infinitely differentiable solution, a PS method would be expected to exhibit geometric or supergeometric convergence for large J [1, 2]. Indeed, it can be seen in Panel b that geometric convergence is obtained for the smooth KdV solution. For the two-fluid model, on the other hand, only subgeometric convergence is achieved due to the developing shock discontinuity in the solution. Nevertheless, as Figure 4 demonstrates, such a subgeometric exponential convergence rate is still much faster than the conventional algebraic convergence rates. Finally, note that the tolerance in the Runge–Kutta solver for these simulations was set to 10^{-14} (restricted by machine precision). Further grid refinement would thus cause the PS curve to level out, and no additional gain in accuracy would be achieved.

4.2. Computational time

For the prediction of multiphase flow in pipelines, the point of using highly accurate numerical schemes is not to reduce the numerical error to machine precision. It is rather to reduce the number of grid points and time steps necessary to resolve the physics to a level of detail consistent with the model assumptions. Figure 5 illustrates this point. In Panel a, the final holdup profiles of the PS and the first-order FD method from the previous subsection are replotted. In addition, three more refined solutions with the first-order method are included. To obtain the same level of accuracy with the first-order method as with the PS method with 64 grid points, the graph indicates that a roughly 300 times finer mesh must be used. Naturally, such a refinement is expensive in terms of both memory and computational time. For these particular simulations, the computational time for the PS method was only 5% higher than that for the first-order method with the same refinement. The computational time for the first-order method with 20 000 grid points, on the other hand, was more than 10 000 times higher. In other words, a reduction in the computational time by four orders of magnitude was obtained by using the PS method instead of the widespread first-order method with comparable accuracy.

Panel b in Figure 5 demonstrates an effect of the integrating factor, which is especially important when solving problems involving higher order derivatives. Since the two-fluid model defined by (7) contains only first-order derivatives, the KdV simulation case from the previous subsection is used for illustration. Note, however, that there exist many two-fluid model formulations that include higher order derivatives, for which this effect is highly relevant. The graph in Figure 5(b) displays

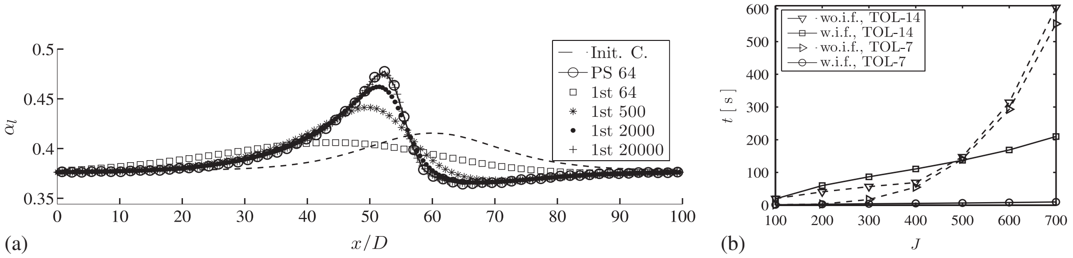

Figure 5. Panel a: Holdup profiles after the initial wave in the two-fluid model simulations has been propagated about $200D$. Panel b: Computational time as a function of the number of grid points for the KdV equation. The PS method with (w.i.f.) and without (wo.i.f.) the integrating factor is used combined with tolerances corresponding to $\mathrm{TOL}=10^{-7}$ and 10^{-14}. The computations were performed with an Intel Pentium M 2.0 GHz processor.

a comparison of the computational time for the PS method with (w.i.f.) and without (wo.i.f) the integrating factor. All simulations have been run twice with the tolerance in the Runge–Kutta solver set to $\mathrm{TOL}=10^{-7}$ and 10^{-14}, respectively. For the simulations with coarser grids, it is clear that the tolerance governs the computational time. As the grid is refined, however, the computational time increases dramatically for the simulations without the integrating factor regardless of the tolerance level. This increase can be explained by considering the linear stability of the numerical method. Owing to the third-order derivative in (9), linear stability normally requires that the time step size varies with the number of grid points as $\Delta t \propto J^{-3}$. In the simulations including the integrating factor, on the other hand, the linear parts of the problem are solved analytically. Thus, the method is unconditionally linearly stable, and much longer time steps can be used. Although each time step with the integrating factor demands a little extra work, the net result for refined grids is still a substantial save in the total computational time.

Finally, we would like to point out that the integrating factor approach increases accuracy and stability for problems not including higher order derivatives as well. Although the effect is not as pronounced as in Figure 5(b), the computational efficiency can be significantly improved, particularly for stiff problems that are dominated by linear terms. All in all, the combination of a more accurate spatial discretization, the analytic solution of linear terms, and the optimized time-integrator thus provides a substantial reduction in computational time for our PS method compared with conventional numerical methods.

4.3. Linear stability

This subsection investigates the ability of the PS method to reproduce the physical linear stability properties of the two-fluid model. A Kelvin–Helmholtz stability analysis has been carried out by first perturbing the steady-state solution with Fourier modes on the form $\exp[\mathrm{i}(kx-\omega t)]$ with k denoting the wave number and ω denoting the frequency. Thereafter, the system is linearized and the resulting dispersion relation is solved for the amplification factors, $\mathrm{Im}(\omega)$. Positive amplification factors indicate unstable conditions and *vice versa*. Three simulation cases referred to as Cases a, b and c have been selected. As initial conditions, all cases use a small-amplitude, long-wavelength sinusoidal perturbation with a wavelength, λ, that covers the full length of the computational domain ($100D$). The flow rates are indicated in the flowchart in Figure 6(a) together with the simulation case used in the previous analysis and the viscous (VKH) and inviscid (IKH) Kelvin–Helmholtz lines. Cases a, b and c are situated right above, on, and directly below the VKH line, which constitutes the linear neutral stability criterion for the two-fluid model. The initial perturbation is propagated about 25 wavelengths, and the amplitude of the holdup (amp_α) is monitored to investigate the evolution of the wave. The amplitude is calculated at each time step by taking the Fourier transform of the holdup vector and extracting the magnitude of the Fourier component corresponding to the wavelength of the initial perturbation ($\lambda=100D$).

Panel b in Figure 6 shows the evolution of the normalized amplitude for the PS and the first-order FD methods with 64 grid points. The initial decrease in amplitude observed for all simulation cases is due to the fact that the sinusoidal wave is not a solution to the two-fluid model. It thus takes some time for the long-term trends of the simulations to be established. Apart from this initial disturbance, the PS method predicts the wave to behave as anticipated based on the linear stability criterion. In Case a, the wave slowly grows until the amplitude is a bit more than doubled at the end of the simulation. Furthermore, the wave amplitude remains constant in Case b and decreases slowly in Case c. For the first-order method, on the other hand, numerical diffusion

DOI: 10.1002/fld

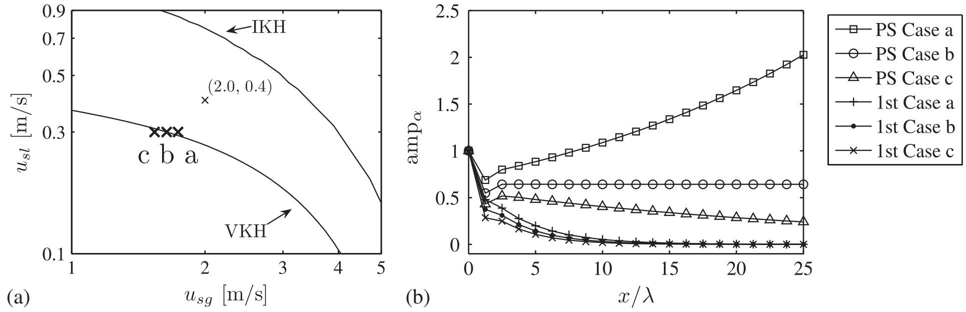

Figure 6. Panel a: Flowchart indicating simulation cases a, b and c together with the simulation case used in the previous subsections and the viscous (VKH) and inviscid (IKH) Kelvin–Helmholtz lines. Panel b: The evolution of the normalized wave amplitude as a function of the distance travelled for the different cases simulated with the PS and the first-order FD methods.

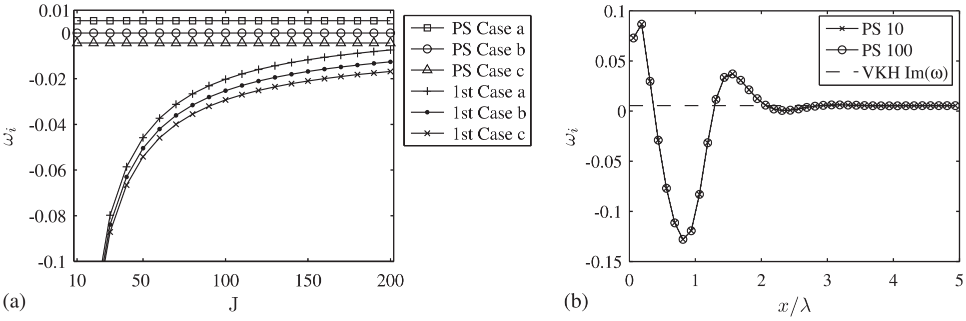

Figure 7. Panel a: Convergence plot of the estimated amplification factor computed after the wave has propagated about eight wavelengths. Panel b: Development of the estimated amplification factor for Case a as a function of wavelengths travelled for two different grid refinements for the PS method compared with the result of the VKH analysis.

totally dominates the behavior. In all three cases, the wave dies out relatively quickly, suggesting that the method predicts the wrong qualitative behavior of the two-fluid model.

Figure 7 compares an estimated amplification factor obtained from the nonlinear simulations, ω_i, with the amplification factor from the linear VKH analysis, $\mathrm{Im}(\omega)$. The estimated amplification factor is computed with the relation

$$\omega_\mathrm{i}\left(\frac{t_n+t_{n-1}}{2}\right)=\frac{\ln\left(\dfrac{\mathrm{amp}_\alpha(t_n)}{\mathrm{amp}_\alpha(t_{n-1})}\right)}{t_n-t_{n-1}} \tag{23}$$

For Cases a, b and c, the VKH analysis yields amplification factors of $5.4\times10^{-3}\,\mathrm{s}^{-1}$, $0.0\times10^{-3}\,\mathrm{s}^{-1}$ and $-4.4\times10^{-3}\,\mathrm{s}^{-1}$, respectively. In Figure 7(a), ω_i at the time when the initial perturbation has travelled about eight wavelengths is plotted *versus* the grid refinement. While the first-order method substantially underpredicts the amplification factor even with 200 grid points per wavelength, the PS method provides accurate predictions with much coarser grids. In fact, the PS method with only 10 grid points yields an estimated amplification factor that in each case is less than $10^{-5}\,\mathrm{s}^{-1}$ different from the value predicted by the linear analysis. Figure 7(b) shows the development of ω_{i} in the initial part of simulations of Case a with two different refinements of the PS method. In both simulations, the estimated amplification factor has converged to a value very close to the value obtained from the VKH analysis when the wave has travelled about three wavelengths. Furthermore, it is noteworthy that the PS method with 10 and 100 grid points yields almost identical results. This behavior is readily explained by the fact that most of the operations in PS methods are performed in Fourier space, in which the variables are represented by trigonometric series. Since these particular simulations are only weakly nonlinear and since the initial conditions contain only one frequency, not much is gained by adding extra grid points beyond the amount required to resolve this frequency.

The results in this section illustrate the importance of using sufficiently accurate numerical methods when testing the performance of wave models. Only in this way, one can be sure that the numerical results reflect the true nature of the physical models. Furthermore, it has been demonstrated that for sufficiently smooth solutions, the proposed PS method provides the desired accuracy at substantially lower computational cost compared with conventional FD-based schemes.

5. CONCLUSION

A pseudospectral (PS) Fourier method has been developed for the simulation of waves in multiphase pipe flow. The numerical method is implemented for a standard 1D incompressible two-fluid model, and it is based on mathematical reformulations combined with extensive use of FFTs. First, the linear parts of the problem are extracted and solved analytically by using a change of variables involving an integrating factor. Thereafter, the nonlinear parts are transformed into Fourier space, in which their spatial derivatives are calculated by a simple multiplication. In order to avoid aliasing errors due to the discrete computation of nonlinear terms, the high-frequency part of the solution spectrum is padded with zeros. The resulting, nonlinear equations are advanced in time using a fifth-order Runge–Kutta algorithm with an adaptive step size control. Finally, the physical variables at the next time step is obtained by reversing the change of variables and applying an inverse FFT.

The simulations presented in Section 4 compare our PS method with conventional schemes based on finite difference (FD) discretizations of orders 1, 2, 4 and 6. Besides the simulations of the incompressible two-fluid model, the simpler KdV equation is used to verify the reliability of the implementation and the performance of the numerical method. The rapid exponential convergence rate of the PS method is demonstrated by the means of a grid refinement analysis. The unparalleled accuracy combined with the unconditional linear stability of our PS algorithm opens for vast reductions in computational time. For a simple wave propagation case, the computational cost is cut by four orders of magnitude compared with the first-order method. Note that such first-order methods constitute the industrial standard in present multiphase flow simulators. Finally, three simulation cases close to the linear neutral stability criterion of the two-fluid model are presented. In contrast to the first-order method, the PS method reproduces the anticipated behavior in all cases even with a relatively coarse grid.

All in all, the simulations demonstrate that our PS method is able to very accurately and effectively capture the evolution of waves. It is virtually free of both dissipative and dispersive errors making it possible to reduce the number of grid points and thus the computational time to a minimum. Furthermore, the algorithm is easily extended to include new terms and is therefore, in our opinion, an ideal tool for testing improvements in the description of waves in two-fluid models.

APPENDIX A: FRICTION MODEL

The friction model is defined by the following correlations, where s indicates the wetted perimeters and subscript f=l,g represents the liquid and the gas phases, respectively. More details on the model can be found in Espedal [19].

Shear stresses are given by

$$\tau_f \equiv \tfrac{1}{8} f_f \rho_f u_f |u_f| \quad \text{and} \quad \tau_{\mathrm{i}} \equiv \tfrac{3}{8} f_{\mathrm{g}} \rho_{\mathrm{g}} (u_{\mathrm{g}} - u_{\mathrm{l}}) |u_{\mathrm{g}} - u_{\mathrm{l}}| \tag{A1}$$

Friction factors are given by

$$f_f \equiv \max \left\{ \left[1.8 \log_{10} \left(\frac{6,9}{Re_f} \right) + \left(\frac{\varepsilon}{3.7 D_{\mathrm{H},f}} \right)^{1.11} \right]^{-2}, \frac{64}{Re_f} \right\} \tag{A2}$$

Reynolds numbers are given by

$$Re_f \equiv \frac{\rho_f u_f D_{\mathrm{H},f}}{\mu_f} \tag{A3}$$

Hydraulic diameters

$$D_{\mathrm{H,l}} \equiv \frac{4\alpha_{\mathrm{l}} A}{s_{\mathrm{l}}} \quad \text{and} \quad D_{\mathrm{H,g}} \equiv \frac{4\alpha_{\mathrm{g}} A}{s_{\mathrm{g}} + s_{\mathrm{i}}} \tag{A4}$$

In this paper the wall roughness, ε, has been set to 2×10^{-5} m.

APPENDIX B: CNOIDAL WAVE

The cnoidal wave, which is an analytical travelling wave solution to the KdV equation, is given by

$$\eta = a \frac{[\mathrm{dn}^2(\kappa\theta, m)] - E/K}{1 - E/K} \tag{B1}$$

where a denotes the amplitude relative to the mean surface level and $m \in [0, 1]$ is a parameter that controls the shape of the wave. For small m, (B1) becomes sinusoidal, whereas in the limit $m \to 1$ (B1) becomes a solitary wave. K and E are the complete elliptic integrals of the first and second kinds, respectively, and dn is the Jacobi elliptic function. The coordinate θ is defined by $\theta \equiv x - ct - \delta$, where δ is the constant phase shift. The wave speed, c, is calculated using

$$c = \sqrt{gh_0} \left[1 + \frac{a(2 - m - 3E/K)}{2h(1 - E/K)} \right] \tag{B2}$$

Finally, κ is given by $\kappa \equiv 2K/\lambda$ where λ denotes the wavelength.

APPENDIX C: LINEAR AND NONLINEAR OPERATORS

The elements in the linear operator $\hat{\mathbb{L}}$ are given by

$$\hat{l}_{11} \equiv \left[\alpha_{\mathrm{l}0} \left(\frac{\partial u_{\mathrm{l}}}{\partial \alpha_{\mathrm{l}}} \right)_{\mathbf{\Psi}_0} + u_{\mathrm{l}0} \right] \mathrm{i}k \tag{C1}$$

$$\hat{l}_{12} \equiv \alpha_{\mathrm{l}0} \left(\frac{\partial u_{\mathrm{l}}}{\partial v} \right)_{\mathbf{\Psi}_0} \mathrm{i}k \tag{C2}$$

$$\hat{l}_{21} \equiv \left[\rho_{\mathrm{l}} u_{\mathrm{l}0} \left(\frac{\partial u_{\mathrm{l}}}{\partial \alpha_{\mathrm{l}}} \right)_{\mathbf{\Psi}_0} - \rho_{\mathrm{g}} u_{\mathrm{g}0} \left(\frac{\partial u_{\mathrm{g}}}{\partial \alpha_{\mathrm{l}}} \right)_{\mathbf{\Psi}_0} + (\rho_{\mathrm{l}} - \rho_{\mathrm{g}}) g \cos\beta \left(\frac{\partial h_{\mathrm{l}}}{\partial \alpha_{\mathrm{l}}} \right)_{\mathbf{\Psi}_0} \right] \mathrm{i}k \tag{C3}$$

$$\hat{l}_{22} \equiv \left[\rho_{\mathrm{l}} u_{\mathrm{l}0} \left(\frac{\partial u_{\mathrm{l}}}{\partial v} \right)_{\mathbf{\Psi}_0} - \rho_{\mathrm{g}} u_{\mathrm{g}0} \left(\frac{\partial u_{\mathrm{g}}}{\partial v} \right)_{\mathbf{\Psi}_0} \right] \mathrm{i}k \tag{C4}$$

and the elements in the nonlinear operator $\hat{\mathbf{N}}$ are defined by

$$\hat{n}_1(\mathbf{\Psi}') \equiv [-\widehat{(u_{\mathrm{l}}'\alpha_{\mathrm{l}}')} - \alpha_{\mathrm{l}0}\widehat{R_{u_{\mathrm{l}}}}]\mathrm{i}k \tag{C5}$$

$$\hat{n}_2(\mathbf{\Psi}') \equiv [-\rho_{\mathrm{l}} u_{\mathrm{l}0}\widehat{R_{u_{\mathrm{l}}}} - \tfrac{1}{2}\rho_{\mathrm{l}}\widehat{u_{\mathrm{l}}'^2} + \rho_{\mathrm{g}} u_{\mathrm{g}0}\widehat{R_{u_{\mathrm{g}}}} + \tfrac{1}{2}\rho_{\mathrm{g}}\widehat{u_{\mathrm{g}}'^2} - (\rho_{\mathrm{l}} - \rho_{\mathrm{g}}) g \cos\beta \widehat{R_{h_{\mathrm{l}}}}]\mathrm{i}k + \widehat{S} \tag{C6}$$

The expressions for the derivatives in $\hat{\mathbb{L}}$ are obtained analytically using the two algebraic relations (4) and (5), and the subscript $\mathbf{\Psi}_0$ indicates that they should be evaluated at the steady-state conditions. R_γ represents the remainder of a first-order Taylor expansion of γ', and it is defined by

$$R_\gamma \equiv \gamma' - \alpha_{\mathrm{l}}' \left(\frac{\partial \gamma}{\partial \alpha_{\mathrm{l}}} \right)_{\mathbf{\Psi}_0} - v' \left(\frac{\partial \gamma}{\partial v} \right)_{\mathbf{\Psi}_0} \tag{C7}$$

APPENDIX D: ELEMENTS IN $\mathbb{E}_\pm$

The elements in the integrating factor matrixes $\mathbb{E}_\pm$ are defined by

$$e_{\pm 11} \equiv \tfrac{1}{2} e^{\pm 1/2\check{t}(\hat{l}_{11}+\hat{l}_{22})} [2\cosh(\pm\tfrac{1}{2}\check{t}\sqrt{d}) \pm \check{t}(\hat{l}_{11} - \hat{l}_{22}) \,\mathrm{sinhc}(\pm\tfrac{1}{2}\check{t}\sqrt{d})] \tag{D1}$$

$$e_{\pm 12} \equiv \check{t} e_{12}^{\pm(\check{t}\sqrt{d}/2)\pm 1/2\check{t}[-\sqrt{d}+\hat{l}_{11}+\hat{l}_{22}]} \hat{l} \,\mathrm{sinhc}(\pm\tfrac{1}{2}\check{t}\sqrt{d}) \tag{D2}$$

$$e_{\pm 21} \equiv \check{t} e_{21}^{\pm(\check{t}\sqrt{d}/2)\pm 1/2\check{t}[-\sqrt{d}+\hat{l}_{11}+\hat{l}_{22}]} \hat{l} \,\mathrm{sinhc}(\pm\tfrac{1}{2}\check{t}\sqrt{d}) \tag{D3}$$

$$e_{\pm 22} \equiv \tfrac{1}{2} e^{\pm 1/2\check{t}(\hat{l}_{11}+\hat{l}_{22})} [2\cosh(\pm\tfrac{1}{2}\check{t}\sqrt{d}) \pm \check{t}(-\hat{l}_{11} + \hat{l}_{22}) \,\mathrm{sinhc}(\pm\tfrac{1}{2}\check{t}\sqrt{d})] \tag{D4}$$

where the $\hat{l}_{ij}$ are the elements of the linear matrix given in Appendix C. Furthermore, $\check{t} \equiv (t - t_0)$ and the discriminant $d \equiv 4\hat{l}_{12}\hat{l}_{21} + (\hat{l}_{11} - \hat{l}_{22})^2$. Finally, the function $\mathrm{sinhc}(x)$ is used in order to remove apparent singularities for $\check{t}\sqrt{d} = 0$. In general, it is in defined as

$$\mathrm{sinhc}(x) \equiv x^{-1}\sinh(x), \quad |x| > 5 \times 10^{-3} \tag{D5}$$

while for small x a fourth-order Taylor series expansion is used to redefine the function as

$$\text{sinhc}(x) \equiv 1 + x^2\left(\tfrac{1}{6} + \tfrac{1}{120}x^2\right), \quad |x| < 5\times 10^{-3} \tag{D6}$$

which is accurate to machine double precision.

ACKNOWLEDGEMENTS

This work is part of the Horizon Joint Industry Program (JIP) at the Institute for Energy Technology (IFE) and Scandpower Petroleum Technology (member of SPT Group). The Horizon JIP is sponsored by ENI, ExxonMobil, Statoil, Shell, Chevron, Hydro and SPT Group. The financial support from the Center for Biomedical Computing at the Simula Research Laboratory is also acknowledged.

REFERENCES

1. Canuto C, Hussaini MY, Quarteroni A, Zang TA. *Spectral Methods*: *Fundamentals in Single Domains*. Springer: Berlin, Germany, 2006.
2. Boyd JP. *Chebyshev and Fourier Spectral Methods*. Dover: New York, U.S.A., 2001.
3. Fornberg B. *A Practical Guide to Pseudospectral Methods*. Cambridge University Press: New York, U.S.A., 1998.
4. Galerkin B. Rods and plates: series occurring in various questions concerning the elastic equilibrium of rods and plates. *Vestnik Inzhenerov* 1915; **19**:897–908.
5. Kreiss HO, Oliger J. Comparison of accurate methods for the integration of hyperbolic equations. *Tellus* 1972; **24**:119–215.
6. Orszag SA. Comparison of pseudospectral and spectral approximations. *Studies in Applied Mathematics* 1972; **51**:253–259.
7. Canuto C, Maday Y, Quarteroni A, Zang TA. *Spectral Methods. Evolution to Complex Domains and Applications to Fluid Dynamics*. Springer: New York, U.S.A., 2007.
8. Johnson GW. A study of stratified gas–liquid pipe flow. *Ph.D. Thesis*, Faculty of Mathematics and Natural Sciences, University of Oslo, Norway, 2005.
9. Barnea D, Taitel Y. Non-linear interfacial instability of separated flow. *Chemical Engineering Science* 1994; **49**:2341–2349.
10. Larsen M, Hedne P. Three phase slug tracking with PeTra. *Engineering Technology Conference on Energy*, Houston, U.S.A., 2001; 765–775.
11. Pauchon C, Dhulesia H, Lopez D, Fabre J. TACITE: a comprehensive mechanistic model for two-phase flow. *Sixth International Conference on Multiphase Production*, Cannes, France, BHR Group, 1993; 29–50.
12. Bendiksen KH, Malnes D, Moe R, Nuland S. Dynamic two-fluid model OLGA. Theory and application. *SPE Production Engineering* 1991; **6**:171–180.
13. Omgba-Essama C. Numerical modelling of transient gas–liquid flows. *Ph.D. Thesis*, Cranfield University, U.K., 2004.
14. Issa RI, Kempf MHW. Simulation of slug flow in horizontal and nearly horizontal pipes with the two-fluid model. *International Journal of Multiphase Flow* 2003; **29**:69–95.
15. Fructus D, Clamond D, Grue J, Kristiansen Ø. An efficient model for three-dimensional surface wave simulations. Part I: free space problems. *Journal of Computational Physics* 2005; **205**:665–685.
16. Watson M. Non linear waves in pipeline two-phase flows. *Proceedings of the 3rd International Conference on Hyperbolic Problems*, Uppsala, Sweden. Studentlitteratur: Lund, 1990; 938–956.
17. Barnea D, Taitel Y. Kelvin–Helmholtz stability criteria for stratified flow: viscous versus non-viscous (inviscid) approaches. *International Journal of Multiphase Flow* 1993; **19**:639–649.
18. Andritsos N, Hanratty TJ. Interfacial instabilities for horizontal gas-liquid flows in pipelines. *International Journal of Multiphase Flow* 1987; **13**:583–603.
19. Espedal M. An experimental investigation of stratified two-phase flow at small inclinations. *Ph.D. Thesis*, Norwegian University of Science and Technology, 1998.
20. Mei CC. *The Applied Dynamics of Ocean Surface Waves*. World Scientific: Singapore, 1989.

DOI: 10.1002/fld

21. Korteweg DJ, de Vries F. On the change of form of long waves advancing in a rectangular canal, and on a new type of long stationary waves. *Philosophical Magazine* 1895; **39**:422–443.
22. Fornberg B, Whitham GB. A numerical and theoretical study of certain nonlinear wave phenomena. *Philosophical Transactions of the Royal Society of London, Series A* 1978; **289**:373–404.
23. Kreyzig E. *Advanced Engineering Mathematics*. Wiley: Singapore, 1999.
24. Hairer E, Nørsett SP, Wanner G. *Solving Ordinary Differential Equations I*: *Nonstiff Problems*. Springer: Berlin, Germany, 2000.
25. Clamond D, Fructus D, Grue J. A note on time integrators in water wave simulations. *Journal of Engineering Mathematics* 2007; **58**(8):149–156.
26. Dormand JR, Prince PJ. A family of embedded Runge–Kutta formulae. *Journal of Computational and Applied Mathematics* 1980; **6**:19–26.
27. Hairer E, Wanner G. *Solving Ordinary Differential Equations II*: *Stiff and Differential–Algebraic Problems*. Springer: Berlin, Germany, 2002.
28. Gustafsson K. Control theoretic techniques for stepsize selection in explicit Runge–Kutta methods. *ACM Transactions on Mathematical Software* 1991; **17**:533–554.

DOI: 10.1002/fld